IEEE Access
Multidisciplinary | Rapid Review | Open Access Journal

Received February 25, 2020, accepted March 13, 2020, date of publication March 20, 2020, date of current version April 10, 2020.

Digital Object Identifier 10.1109/ACCESS.2020.2982250

Novel Framework for Optical Film Defect Detection and Classification

NGOC TUYEN LE[1], JING-WEIN WANG[1], MENG-HSIANG SHIH[1], AND CHOU-CHEN WANG[2]

[1]Institute of Photonics Engineering, National Kaohsiung University of Science and Technology, Kaohsiung 80778, Taiwan
[2]Department of Electronic Engineering, I-Shou University, Kaohsiung 84001, Taiwan

Corresponding author: Jing-Wein Wang (jwwang@nkust.edu.tw)

This work was supported in part by the Ministry of Sciences and Technology, Taiwan, under Grant MOST 108-2218-E-992-319.

ABSTRACT Currently, liquid crystal displays (LCDs) are the most popular type of flat panel display and are used in most applications. An LCD contains many critical optical film components that are produced in highly automated and precisely monitored facilities throughout the complex manufacturing process. However, defect detection and classification through visual inspection is very difficult during the manufacturing process. To overcome this problem, a novel framework based on machine vision known as the optical film defect detection and classification system is presented for use in the real-time inspection. First, an image acquisition system equipped with a high-resolution camera and custom-made lighting field was designed to obtain a high-quality optical film image. Second, the defects on an optical film were detected using localized cross-projection based on proposed adaptive energy analysis. Finally, the defect images were classified into four types by using the developed classification algorith—point, scratch, foreign material, and stain. The quality of the products yielded after defect detection and classification of the optical film was compared with the standard product quality of the manufacturer. Experiments were conducted using samples collected from the largest manufacturer in Taiwan to validate the performance of the proposed framework. The accurate defect detection rate is 99.6%, the classification accuracy rate is 100%, and the total operation time is short whichonly 6.129s are required on average to perform the inspection for an optical film sample. The results demonstrate that the proposed method is sound and useful for optical film inspection in industries.

INDEX TERMS Optical film, automatic optical inspection, color space, adaptive energy analysis, cross-projection, Kirsch operator, bit-plane slicing, support vector machine.

I. INTRODUCTION

Currently, liquid crystal displays (LCDs) are the most popular flat panel displays that have replaced traditional cathode ray tube displays in most applications and become the mainstream electronic display. An LCD is a device that utilizes the electro-optical characteristics of a liquid crystal to convert an electrical stimulus into a visual signal. Due to the complicated manufacturing process and expensive equipment, the LCD manufacturing industry is highly competitive. An LCD contains many critical optical film components, such as a reflector sheet, light guide plate (LGP), diffuser sheet, prism sheet, bottom polarizer, a bottom glass substrate (backplane), and thin-film transistor. Each component inside an LCD has a crucial role in ensuring LCD quality. Therefore, highly automated and precisely monitored facilities are used throughout the complex manufacturing process.

The associate editor coordinating the review of this manuscript and approving it for publication was Donato Impedovo.

Visual defect inspection serves a pivotal role in the LCD manufacturing process. However, the optical film industry currently lacks an efficient defect inspection system, and detection and classification are conducted and recorded manually. Therefore, defect images are identified by experienced engineers or operators. However, this visual inspection method includes the following drawbacks: high time consumption, subjective and hence variable defect detection, and human fatigue that leads to misrecognition. In contrast to human inspection, machine-vision-based techniques have advantages such as high efficiency, low cost, and objectivity and are widely applied for industrial defect inspection. The automatic optical inspection system (AOI) is a key machine-vision-based technique in industry 4.0 that is used for manufacturing and testing products to ensure that high-quality products are obtained from the production line and the items are manufactured correctly without fault. AOI is an essential tool that employs optics to capture images of an object that is being tested using an integrated test strategy and ensures

that costs are kept as low as possible by detecting faults early in the production line. AOI has been increasingly used for automatic defect detection in several industrial fields for the quality control of products, such as printed circuit boards [1]–[3], plastic products [4], steel products [5], [6], glass products [7], [8], solar cells [9], [10], textiles and garments [11]. Besides, AOI has also been used for counting blister cards within drug packages [12] and checking the surface of the lithium-ion battery electrode [13].

Various methods have been developed for defect inspection of LCDs in the past decade based on machine vision. Based on the monotonical relation of 3D sizes and grayscale value of microdefects, Deng *et al.* [14] used the support vector regression (SVR) algorithm to develop a vision-based 3D shape measurement system for detecting and measuring the transparent micro defects on the polarizing film. Kuo *et al.* [15] used Fourier transform to detect and enhance defects on polarizing films, which are the key component in LCDs. Then, they extracted various features, such as maximum gray level, eccentricity, contrast, and homogeneity of the gray level co-occurrence matrix, from the defect images and input them in the radial basis function neural network and backpropagation neural network (BPNN) for classification. To improve the inspection quality of polymeric polarizers in thin-film transistor LCD (TFT-LCD) panels, Lai *et al.* [16] used an LCD monitor as a structured light source to display the binary stripe pattern of a polymeric polarizer before capturing its images. Then, they used the robust principal component analysis algorithm for processing and characterizing the defect images. Gan and Zhao [17] proposed a modified local binary fitting model to initialize contour and competent features for the extraction of defect boundaries. Tsai *et al.* [18] proposed an automatic quantization of Mura panel defects in terms of the crossing points of the interference pattern to detect gap defects before injecting liquid crystals into the cells of a TFT-LCD panel. For pretesting gap defects on a TFT-LCD panel, Li *et al.* [19] proposed an optical interference pattern-sensing method to detect the defects and then use the neural network method to identify the types of defects. To detect Mura defects on an LCD, Wang *et al.* [20] used the first four singular values of the images captured to divide the defect images into the following two categories—coarse and fine. Then, they adopted two-dimensional (2D) discrete wavelet coefficients combined with region growing to extract defect regions. Li and Tsai [21] proposed a Hough transform method for all individual row and column gray-level profiles to identify Mura defects in LCD panels, which can be presented in the 2D inspection image. Chen *et al.* [22] proposed a neural network with different learning methods such as backpropagation (BP), radial basis function (RBF), learning vector quantization 1 (LVQ1), and learning vector quantization 2 (LVQ2) for defect recognition. Bi *et al.* [23] first eliminated global textured backgrounds and then used the Chan-Vese model for segmenting Mura defects for TFT-LCD panels. Chen and Chou [24] used discrete wavelet transform and discrete cosine transform to detect blob Mura defects

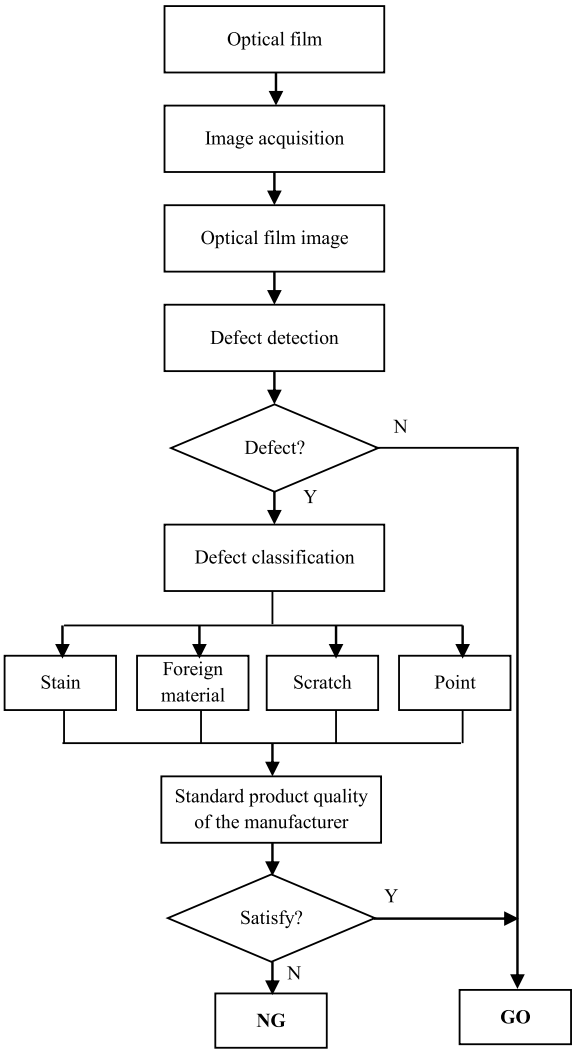

FIGURE 1. The overall of the automated optical film defect detection and classification system (OFDDCS).

on TFT-LCD panels. Lee and Yoo [25] first used modified regression diagnostics and Niblackthresholding to segment the candidate Mura defect regions from a TFT-LCD panel image and then quantified the Mura defect level for each candidate region based on human eye sensitivity. In spite of many kinds of researches proposed for detecting defects on the LCD screen or the polarizing film, which are the key component of LCD panels, most methods are only focused on defect detection.

In this study, we propose a high-precision automated optical film defect detection and classification system (OFDDCS), which is based on machine vision for use in real-time detection and classification. Our proposed system is applicable to different components of the optical film, such as reflector sheet, diffuser sheet, and LGP. The overall flowchart of OFDDCS is shown in Fig. 1. First, we designed an image acquisition system equipped with a high-resolution camera and custom-made lighting field to obtain high-quality optical film images. Second, the defects on the optical film were detected by adopting localized cross-projection based on the

proposed adaptive energy analysis method. Finally, the defect images were classified into the following four types of defects by the proposed classification algorithm—point, scratch, foreign material, and stain. The quality of the products obtained after defect detection and classification of the optical film was compared with the standard product quality of the manufacturer. Optical films provided by a company in Taiwan were used for experiments to demonstrate that the proposed method is sound and useful for optical film inspection in industries. Our proposed method not only reduces the number of human inspectors, but also increases the yield rate, and reduces material loss.

The remainder of this paper is organized as follows. Section II describes the image acquisition system. The proposed defect detection method is presented in Section III. Section IV describes the classification algorithm. Section V discusses the experimental results. Finally, the conclusions of this study are presented in Section VI.

II. IMAGE ACQUISITION SYSTEM

This section introduces the system architecture of the optical film inspection apparatus first and then presents particular considerations regarding the illumination scheme. Moreover, the image properties and the challenges of defect detection are discussed.

A. OVERVIEW OF LCD PANEL

An LCD is a device that utilizes the electro-optical characteristics of a liquid crystal to convert an electrical stimulus into a visual signal. The signals help to bring your imagination and ideas to life by displaying them on a screen. In general, an LCD includes some panels that are arranged from top to bottom in the following order: top chassis, top polarizer, glass substrate, color filter, common electrode, liquid crystal, TFT, glass substrate, bottom polarizer, prism sheet, diffuser sheet, LGP, reflector sheet, and bottom chassis. As shown in Fig.2, we investigated the following three panels and conducted experiments on them in this study: reflector sheet, diffuser sheet, and LGP.

The reflector sheet provides LCD backlight recycling and is often known as a dual brightness enhancement film (DBEF). DBEFs increase on-axis luminance, and thus, more light is available for transmission through the LCD. Typically, one brightness enhancement film (BEF) can increase the brightness level by 40%–60%. Two BEFs are used in some applications for enhancing brightness transmittance. The diffuser sheet is designed to evenly distribute light across the screen to make a solid, evenly lit square and reduce LED hotspots. The LGP is an acrylic panel that is typically fabricated using pure poly (methyl methacrylate) resin, which is extremely transparent and highly weather resistant. This plate is an etched plastic sheet that contains a pattern of bumps that reflect light in a particular direction. An LGP converts a line-shaped light source into a uniform plane-shaped light source. A matrix of lines is etched on the bottom of the LPG panel to direct the light out from the front of the panel, which is known as V cutting. The light that enters the light guide layer from the sides will exit through the front of the layer.

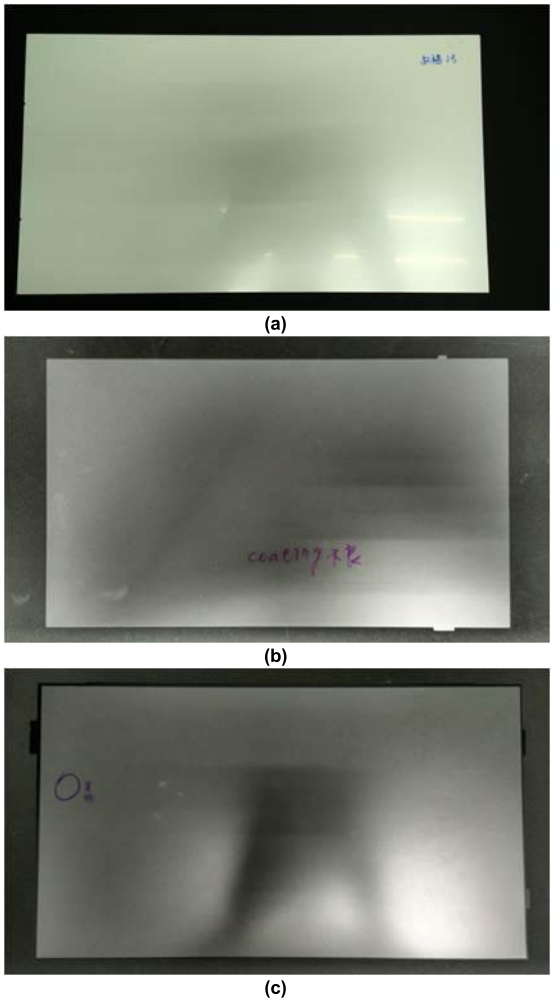

FIGURE 2. LCD panels: (a) Reflector sheet, (b) diffuser sheet, and (c) LGP.

B. IMAGE ACQUISITION SYSTEM

This subsection introduces the system architecture of the optical film inspection apparatus first and presents particular considerations regarding the illumination scheme. Then, the image properties and the challenges of defect detection are discussed.

The lighting setup plays a major role in ensuring the quality of the images acquired using an image acquisition device. This quality is related to the success or failure of the inspection task. When positive light is incident on an object surface, some of the light gets reflected based on the refractive indices of the material on the objects surface, angle of incidence, and medium of the incident light (e.g., air). Conversely, the superfluous light that passes through the object is not only reflected on the front surface but also on the back surface. The light may be reflected back and forth several times, thus capturing images with variable qualities. Therefore, resolving the issue of how to design a suitable image acquisition system for each type of object is crucial in the AOI system. This subsection introduces the components of the proposed image acquisition

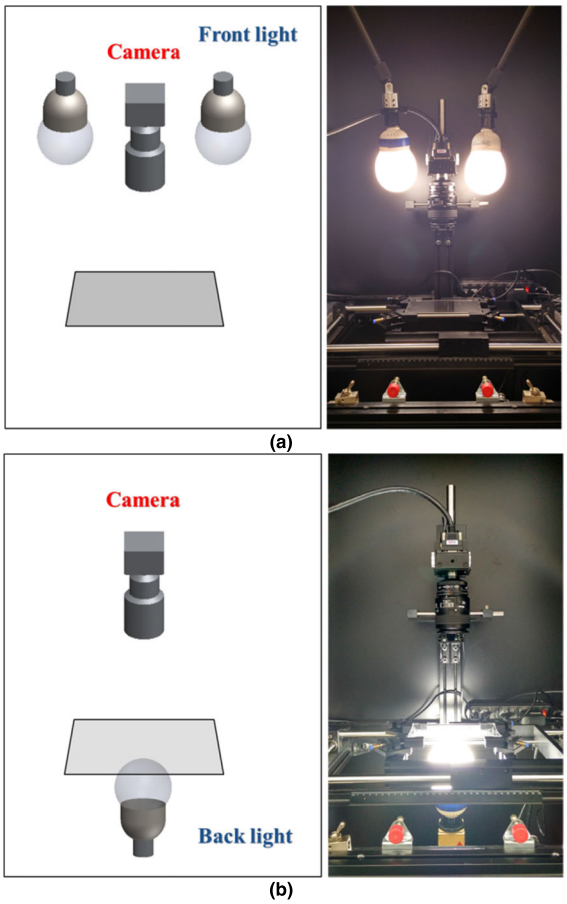

FIGURE 3. A schematic layout of the proposed image acquisition system: (a) front light system applied for reflector sheets and (b) background light system applied for LGP and diffuser sheets.

system, such as the light source setting, camera parameter setting, and image capture design.

To normalize illumination variation and increase the contrast difference between defects and the background, lighting systems, such as background lighting, parallel lighting, and infrared lighting, were used in this study. Before selecting a suitable light source, it is necessary to prioritize the influence of the light source and the type of optical film. Because optical films that are provided by the manufacturer have variable imaging functions, an image set is presented to conduct the image acquisition task.

First, we designed a light source for the reflector sheet. The reflector sheet reflects the light that leaks from the bottom surface of the LGP back into the plate to increase the light usage rate. Thus, front lighting is used for this sheet. However, the main functions of the LGP and diffuser sheet are to provide a uniform surface light source. Thus, background lighting is used. In addition to the light source setting, the distances among light, the camera with lens, and test samples were examined to design an image acquisition system. Fig. 3 displays the proposed optical film image acquisition system. Fig. 3(a) shows the front lighting system used for the reflector sheet and Fig. 3(b) displays the background lighting system used for the LGP and diffuser sheet.

FIGURE 4. Example images of the optical film samples taken using the proposed image acquisition system.

In general, defects of the optical films are small. Thus, it is very difficult to detect them with human eyes. Therefore, image acquisition is a critical step in the defect inspection system. Moreover, we designed an image acquisition system to capture high-resolution images to make defects clearer. Three image examples captured using the proposed system are shown in Fig. 4. This figure displays the optical film images that were examined in this study. The images measure 2, 330 $\times$ 1.750 pixels with a 24-bit BMP format. These images were not only tested for obtaining a high defect detection rate but also reduced in size to decrease the operation time and ensure synchronization with the factory's production line.

III. OPTICAL FILM DEFECT DETECTION

This section introduces the optical film defect detection algorithm. We detected the defect contours by following the defect shape to extract the correct position of the defect in the image. First, the optical film RGB image is converted to YCbCr color space to extract the Y color channel with only 8 bits to reduce the processing time. Next, a smoothing filter was used to smooth the image and enhance the desired local edge and then convert to binary image based on automated Otsu's method [26] to extract the object of interest from the background. After that, localized adaptive energy analysis was used to enhance the defect contour, and then, partial cross-projection was used to cut out the defect image. Finally, the defect is compared to the standard product quality of the manufacturer to determine whether the manufacturer's specification is met. Fig. 5 shows the overall of our defect detection algorithm.

Traditional contour detection is based on edge detection approaches [27], such as Sobel or Canny operator. In such detection approaches, edges are usually extracted by adopting a specific template or using a smooth function. The Sobel edge detector is used for detecting vertical and horizontal edges in an image. However, this detector has a major drawback insofar as it is very sensitive to noise. Moreover, the size of the kernel filter and its coefficients are fixed and cannot be adapted to a given image. Therefore, an adaptive edge detection algorithm is necessary to provide a robust solution that can be adapted to the varying noise levels in the image and to help distinguish between valid image content and visual artifacts introduced by noise. The Canny edge detector is an optimal edge detector that has high performance: high detection accuracy, high localization accuracy, and a unique answer to a true edge. The Canny edge detection algorithm performs better than the Sobel detector and gradient-based operators under almost all scenarios. However, the performance of the Cannyalgorithm primarily depends on adjustable parameters,

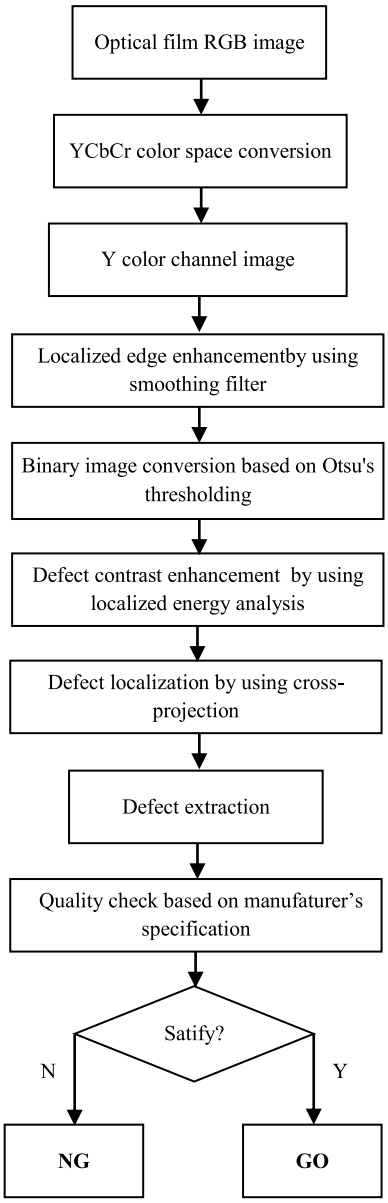

FIGURE 5. Flowchart of the defect detection algorithm.

such as the standard deviation of the Gaussian filter and the threshold value. Recently, an increasing number of edge detection operators have been developed for specific types of edges [28], [29]. Unfortunately, these approaches usually require parameter tuning to adjust sensitivity throughout the image based on the contrast and differences. In this study, the proposed localized energy-based edge detector not only can detect edge pixels in all directions equally well but also has no parameter tuning requirement, has low sensitivity to noise, and has high isotropy.

Contour detection is a technique used for detecting meaningful discontinuities in the gray level and is often used in subsequent image analysis for feature extraction and object recognition. Color is an effective and robust visual cue for distinguishing between objects. Recently, there has been growing interest in color segmentation, which is useful in preliminary processing for many vision-based tasks such as object recognition, visual tracking, and vision-based robotics. However, color variation is encountered in color segmentation due to uneven illumination and the view perspective of a camera. In particular, changing illumination conditions and complex environments containing surfaces or objects with similar colors are major problems that limit the application of color segmentation to visual inspection tasks. The former changes the color characteristics, whereas the latter increases the number of false-positive pixels. The YCbCr color space is often used in digital image processing to take advantage of the lower resolution capability of the human visual system for color with respect to luminosity. In the YCbCr color space, Y is the luma component and Cb and Cr are the blue-difference and red-difference chroma components, respectively. Because defects on an optical film are more sensitive to illumination, we used the luma component Y of the YCbCr color space as a gray level for conducting contour detection. This component is not only more useful for defect detection but also can considerably reduce the processing time. We processed a Y channel image of the YCbCr color space with only 8 bits instead of processing an optical film color image of 24bits, thus reducing the operation time of the proposed system.

Without loss of generality, f is assumed to be an optical film color image with a resolution of $M \times N$, where $f_A, A \in \{R, G, B\}$ represent the RGB color channels.Therefore, $f \in \Re^{M\times N\times N3}$ and $\{f_R, f_G, f_B\} \in \Re^{M\times N}$. The luma component f_Y of f in the YCbCr color space can be computed as follows:

$$f_Y(x, y) = 0.299\, f_R(x, y) + 0.587\, f_G(x, y) + 0.114\, f_B(x, y). \tag{1}$$

Prior to the contour extraction of an object, a smoothing filter was used to smooth the image and enhance the desired local edge. The local standard average μ_Y and energy f_E defined by the mask with 3×3 pixels are expressed in the following equations:

$$\mu_Y = \frac{1}{\eta}\sum_{i=-1}^{1}\sum_{j=-1}^{1} f_Y(x+i, y+j), \tag{2}$$

$$f_E(x, y) = \frac{1}{\eta}\sum_{i=-1}^{1}\sum_{j=-1}^{1} \{f_Y(x+i, y+j) - \mu_Y\}^2, \tag{3}$$

where η is equal to 9 and is a normalizing constant, μ_Y is the average value of the pixels in the mask, and $f_Y(x, y)$ is the luma component of an input image in the YCbCr color space.

A binary image obtained based on an automatic threshold proposed by Otsu [26] was adopted to extract the object of interest from the background. The Otsu algorithm used to obtain the automatic binary threshold τ_{Otsu} is as follows:

$$\tau_{Otsu} = Max\left(\omega_1(\upsilon)\omega_2(\upsilon)[\mu_1(\upsilon) - \mu_2(\upsilon)]^2\right), \tag{4}$$

$$\omega_1(\upsilon) = \sum_{i=0}^{\upsilon-1} p(i), \tag{5}$$

$$\omega_2(\upsilon) = \sum_{i=(\upsilon)}^{255} p(i), \tag{6}$$

FIGURE 6. Defect detection: (a) Original optical film image, (b) Y channel image, (c) localized energy image, (d) localized cross-projection, and (e) defect detection result.

$$\mu_1(\upsilon) = \frac{\sum_{i=0}^{\upsilon-1} p(i) * i}{\omega_1(\upsilon)}, \tag{7}$$

$$\mu_2(\upsilon) = \frac{\sum_{i=(\upsilon)}^{255} p(i) * i}{\omega_2(\upsilon)}, \tag{8}$$

where υ is the current histogram level value from 0 to 255, $\omega_1(\upsilon)$ is the cumulative probability from 0 to $\upsilon - 1$, $\omega_2(\upsilon)$ is the cumulative probability of υ to 255, $\mu_1(\upsilon)$ is the cumulative expected average of 0 to $\upsilon - 1$, $\mu_2(\upsilon)$ is the cumulative expected average of t to 255, and $p(i)$ is the probability of distribution in the image. The binary image based on an automatic threshold value τ_{Otsu}, denoted as f_B, is selected from the energy f_E as follows:

$$f_B(x, y) = \begin{cases} 255, & f_E(x, y) \geq \tau_{Otsu} \\ 0, & otherwise \end{cases}, \tag{9}$$

where pixel values labeled 255 are objects of interest, and pixel values labeled 0 are undesired ones.

Variable types of defects are observed in optical films in the production line. Some defects are minute, and there is a low contrast difference between the defects and background. Thus, the localized energy analysis was adopted to enhance the contrast of the defects in the optical film. The localized energy image f_E of a binary image f_B is calculated as follows:

$$f_E(x, y) = \frac{1}{\eta} \sum_{i=-r}^{r} \sum_{j=-r}^{r} \{f_B(x + i, y + j) - \mu_M\}^2, \tag{10}$$

$$\mu_M = \frac{1}{\eta} \sum_{i=-r}^{r} \sum_{j=-r}^{r} f_B(x + i, y + j), |i| + |j| < \frac{d}{2}, \tag{11}$$

where η is the number of pixels, μ_M is the average value of the pixels in the circular mask M, d is an odd number that is greater than or equal to 3 and expressed as the diameter of the circular mask, and $r = \lfloor \frac{d}{2} \rfloor$ is the radius of the circular mask. The circular mask with a diameter of 5 pixels is presented as follows:

$$M = \begin{bmatrix} & f_B(x, y-2) & \\ f_B(x-1, y-1) & f_B(x, y-1) & f_B(x+1, y-1) \\ f_B(x-2, y) & f_B(x-1, y) & f_B(x, y) \quad f_B(x+1, y) \\ f_B(x+2, y) & f_B(x-1, y+1) & f_B(x, y+1) \\ & f_B(x+1, y+1) \quad f_B(x, y+2) & \end{bmatrix} \tag{12}$$

To fix the exact location of the defect in an optical film, this study adopted the cross-projection method to determine the detection range. The cross-projection method includes two projection mirrors that are used interchangeably to detect marginal points on the contour of the optical film in the image. For a localized energy image f_E, the first projection is known as the forward projection and employs a mask that is denoted as M_1 and that spans from the top left to the bottom right of the image to obtain the maximum value coordinate in the projection. The second projection is known as reverse projection and employs a mask denoted as M_2 that spans from the bottom right point back to the first left point of the image to obtain the minimum value coordinate in the projection. The mask M_1 is defined in Eq. (13), and the mask M_2 is defined in Eq. (14).

$$M_1 = \begin{bmatrix} f_E(x, y) & f_E(x+1, y) & f_E(x+2, y) \\ f_E(x, y+1) & f_E(x+1, y+1) & 0 \\ f_E(x, y+2) & 0 & 0 \end{bmatrix}, \tag{13}$$

$$M_2 = \begin{bmatrix} 0 & 0 & f_E(x, y-2) \\ 0 & f_E(m-1, n-1) & f_E(x, y-1) \\ f_E(x-2, y) & f_E(x-1, y) & f_E(x, y) \end{bmatrix}. \tag{14}$$

Based on the cross-projection results, the defects are automatically extracted to record their numbers, sizes, coordinates, and classification. The manufacturer's specification is then used to determine whether the manufacturer's specification is met. Fig. 6 displays the proposed defect detection method. Fig. 6(a) presents the original optical film used by the proposed acquisition image system. Fig. 6(b) shows the Y color channel of the original image in the YCbCr color space and Fig. 6(c) displays the localized energy image of the image presented in Fig. 6(b). Fig. 6(d) illustrates the results of our localized cross-projection method and Fig. 6(e) shows the defect detection result. The results indicate that the defects are detected accurately.

IV. OPTIC FILM DEFECT CLASSIFICATION

After the defects are extracted using the proposed algorithm, they are classified based on the manufacturer's specifications. As shown in Fig. 7, we can manually classify the defects into the following four types based on our defect detection results—point, scratches, foreign material, and stain. The defects have different sizes, and there is a low contrast difference between the defects and background. Moreover, a tiny defect present in an optical film image may only differ slightly from the surrounding region. All these properties make the inspection extremely difficult. This section proposes an effective method for classifying the defects in the optical film with a high accuracy rate.

First, the defect images are classified into two categories—dark and bright by analyzing the variation of the

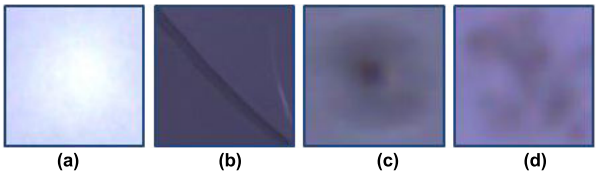

FIGURE 7. Types of defects: (a) point, (b) scratches, (c) foreign material, and (d) stain.

horizontal line passing through the center of the defect image. Next, the defect region is extracted and the background is removed by using the Kirsch operator [30] and energy analysis. At last, the dark category is classified into foreign material and stain defects, whereas the bright category is classified into point and scratch defects. The flowchart of the proposed algorithm is presented in Fig. 8. The detailed algorithm is described in the sub-sections as follows.

A. CLASSIFICATION FOR DARK AND BRIGHT DEFECT IMAGES

Based on our observations, point and scratch defect regions have the characteristic of photosensitivity. Following on lighting effect, these regions have high reflections. This causes a high contrast difference between defects and background. The point and scratch defect images look brighter than the background. By contrast, foreign material and stain defects do not reflect light. Thus, there is a low contrast difference between defect and background. The foreign material and stain defects look darker against the background. Therefore, an algorithm is designed to separate the dark defects from the bright ones.

First, let a horizontal line pass through the center of the defect, as shown in Figs. 9(a) and 10(a). Then, the gray level of the defects crossing this line is computed and is denotedas $\boldsymbol{L_{Gray}}[\boldsymbol{n}]$, where n is the width of the defect image. As shown in Figs. 9(b) and 10(b), we calculated the maximum value coordinate $\boldsymbol{L_{max}}\left(\boldsymbol{x_{max}}, \boldsymbol{y_{max}}\right)$, which is denoted with a red circle in Figs. 9(b) and 10(b), based on the variation in $\boldsymbol{L_{Gray}}[\boldsymbol{n}]$. Moreover, the minimum value coordinate, $\boldsymbol{L_{min}}\left(\boldsymbol{x_{min}}, \boldsymbol{y_{min}}\right)$, that is represented by blue circles in Figs. 9(b) and 10(b) is computed based on the variation in $\boldsymbol{L_{Gray}}[\boldsymbol{n}]$. Then, the line connecting the first point $\boldsymbol{L_{Gray}}[\mathbf{0}]$ and the last point $\boldsymbol{L_{Gray}}[\boldsymbol{n}-\mathbf{1}]$ is denoted as g(x) and represented by a light orange-brown color line in Figs. 9(b) and 10(b), which is the boundary line for classification. The classifier boundary line equation is computed as follows:

$$\boldsymbol{g}(\boldsymbol{x}) = \frac{\boldsymbol{\Delta y}}{\boldsymbol{\Delta x}} \times (\boldsymbol{x} - \boldsymbol{x_0}) + \boldsymbol{y_0}, \tag{15}$$

where $\boldsymbol{\Delta y} = \boldsymbol{y_{n-1}} - \boldsymbol{y_0}$ and $\boldsymbol{\Delta x} = \boldsymbol{x_{n-1}} - \boldsymbol{x_0}$.

Next, the classification of dark or bright defect based on the Euclidean distance of the maximum and minimum points to the classifier boundary line is listed as follows:

$$\boldsymbol{d_1} = \mathbf{d}\left(\boldsymbol{L_{max}}, \boldsymbol{g}(\boldsymbol{x})\right), \tag{16}$$

$$\boldsymbol{d_2} = \mathbf{d}\left(\boldsymbol{L_{min}}, \boldsymbol{g}(\boldsymbol{x})\right), \tag{17}$$

$$\textbf{Defect} = \begin{cases} \textbf{Bright color}, & \boldsymbol{d_1} > \boldsymbol{d_2} \\ \textbf{Dark color}, & \textit{otherwise} \end{cases}. \tag{18}$$

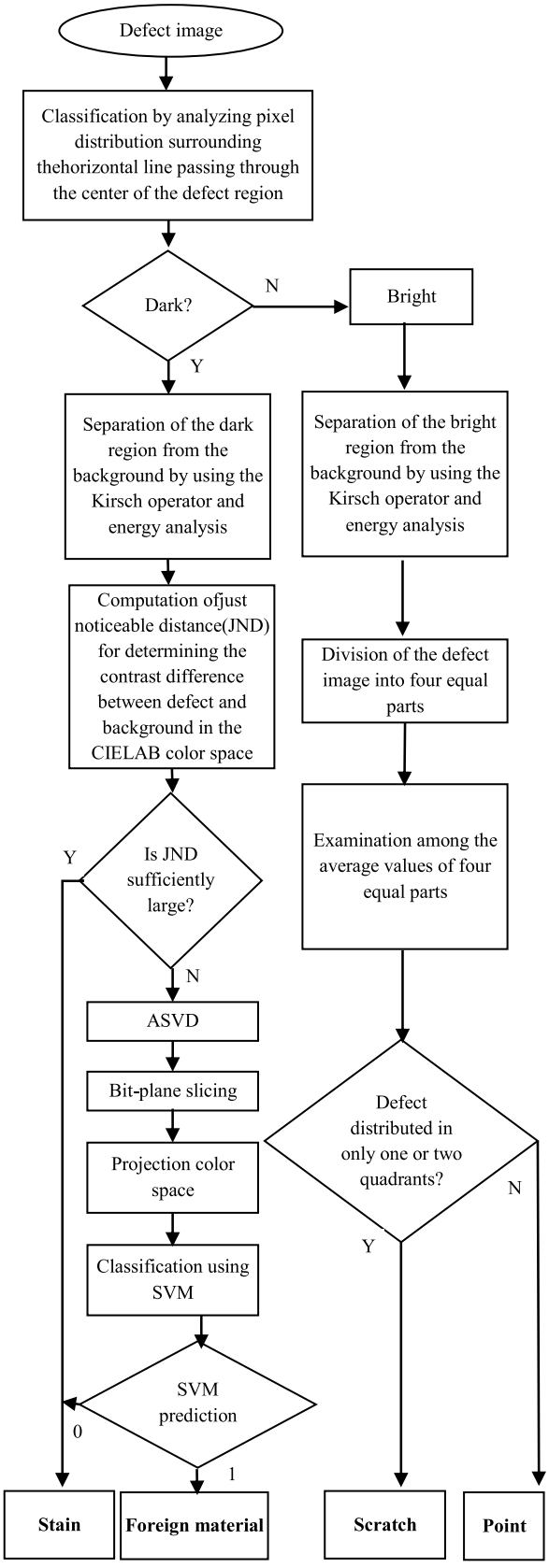

FIGURE 8. Flowchart of the defect classification algorithm.

The examples of the proposed classification are presented in Figs. 9 and 10. In these images, the defect images are

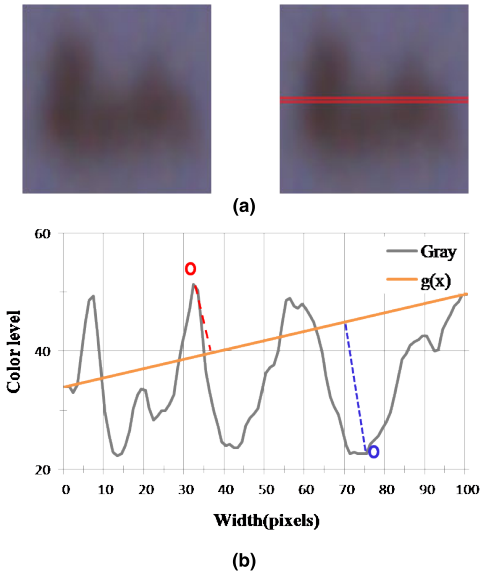

FIGURE 9. Classification algorithm for the dark image: (a) dark defect image and the corresponding horizontal line passing through the center of the defect, and (b) classification chart.

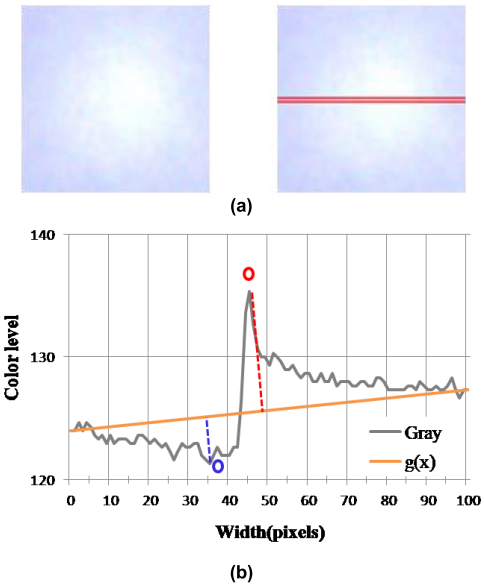

FIGURE 10. Classification algorithm for the bright defect image: (a) bright defect image and the corresponding horizontal line passing through the center of the defect, and (b) classification chart.

classified into two categories: 1) dark defects that include the foreign material and stain defects and 2) bright defects that include the point and scratch defects.

B. ENHANCEMENT OFDEFECT CONTOUR AND BACKGROUND REMOVALOF DEFECT IMAGES

To classify the defect images into the foreign material, stain, point, and scratch defect categories, we have to remove the background of a defect image that contains noise because the noise has a negative effect on the recognition rate of the classification system. Moreover, we used the color defect image, which contains more information compared with the gray defect image, for classification. This subsection presents the method that includes three steps for detecting the edge of a defect in the defect image as follows.

The optical film color image f is first converted to the YCbCr color space by using Eq. (1) to obtain the luma component f_Y. Then, the Kirsch operator is used to detect edges in the image f_Y. The Kirsch operator is a nonlinear edge detector that can detect the maximum edge strength in a few predetermined directions. The Kirsch operator rotates a single kernel mask in 45° increments through eight compass directions: north (N), northwest (NW), west (W), southwest (SW), south (S), southeast (SE), east (E), and northeast (NE). The edge magnitude $\boldsymbol{f_K}$ of the Kirsch operator is calculated as the maximum magnitude across all directions:

$$f_K(x,y) = \max_{z=1,\ldots,8} \sum_{i=-1}^{1} \sum_{j=-1}^{1} g_{ij}^{(z)} \cdot f_Y(x+i, y+j), \quad (19)$$

where z enumerates the eight compass directions N, NW, W, SW, S, SE, E, and NE, respectively, as follows:

$$\boldsymbol{g_{ij}^{(1)}} = \begin{bmatrix} +5 & +5 & +5 \\ -3 & 0 & -3 \\ -3 & -3 & -3 \end{bmatrix}, \quad (20)$$

$$\boldsymbol{g_{ij}^{(2)}} = \begin{bmatrix} +5 & +5 & -3 \\ +5 & 0 & -3 \\ -3 & -3 & -3 \end{bmatrix}, \quad (21)$$

$$\boldsymbol{g_{ij}^{(3)}} = \begin{bmatrix} +5 & -3 & -3 \\ +5 & 0 & -3 \\ +5 & -3 & -3 \end{bmatrix}, \quad (22)$$

$$\boldsymbol{g_{ij}^{(4)}} = \begin{bmatrix} -3 & -3 & -3 \\ +5 & 0 & -3 \\ +5 & +5 & -3 \end{bmatrix}, \quad (23)$$

$$\boldsymbol{g_{ij}^{(5)}} = \begin{bmatrix} -3 & -3 & -3 \\ -3 & 0 & -3 \\ +5 & +5 & +5 \end{bmatrix}, \quad (24)$$

$$\boldsymbol{g_{ij}^{(6)}} = \begin{bmatrix} -3 & -3 & -3 \\ -3 & 0 & +5 \\ -3 & +5 & +5 \end{bmatrix}, \quad (25)$$

$$\boldsymbol{g_{ij}^{(7)}} = \begin{bmatrix} -3 & -3 & +5 \\ -3 & 0 & +5 \\ -3 & -3 & +5 \end{bmatrix}, \quad (26)$$

$$\boldsymbol{g_{ij}^{(8)}} = \begin{bmatrix} -8 & +5 & +5 \\ -5 & 0 & +5 \\ -3 & -3 & -3 \end{bmatrix}. \quad (27)$$

The results of the edge detector are displayed in Fig. 11(b). However, the defect contour is still unclear. In the second step, the adaptive energy analysis that is discussed in Section IV is used to enhance the contour of the defect. The energy image is presented in Fig. 11(c). The defect region is presented in white, and the background is presented in black. In the third step, based on the contour of the defect that is detected in the second step, the color defect region in the image is extracted, as shown in Fig. 11(d). Then, the background is replaced by black. These images are subsequently used for classification.

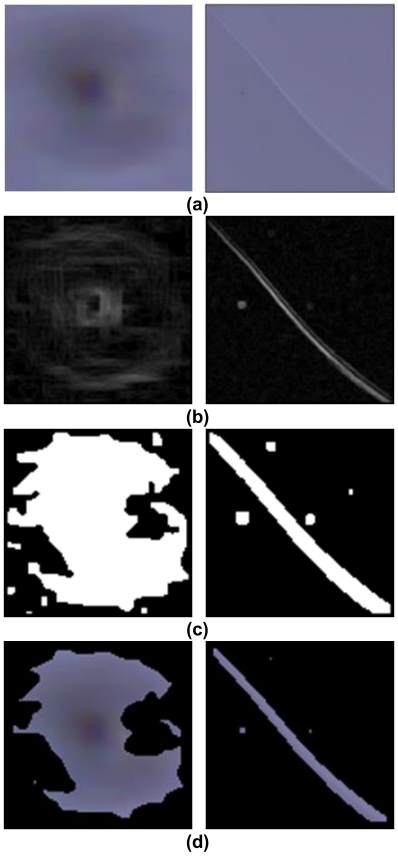

FIGURE 11. Extraction of the defect region and removal of the background in the defect image. (a) defect image, (b) edge detection by the Kirsch operator, (c) energy image, and (d) color defect region in the defect image.

C. CLASSIFY DARK DEFECTS INTO FOREIGN MATERIAL AND STAIN DEFECTS

In the previous section, the background information was removed and assigned to zero. For classification, we focus only on the color region, as shown in Fig. 11(d), that represents the defect region.

Based on the usefulness of the CIELAB color space [31], which describes the most complete color model visible to human eyes, the color defect image is first converted from the RGB color space to the CIELAB color space. The CIELAB color space is derived from the prior master CIE 1931 XYZ color space, which predicts the spectral power distributions that will be perceived as the same color but is not perceptually uniform. To convert the image from the RGB color space to the CIE 1931 XYZ color space, the following equation is employed:

$$\begin{bmatrix} X \\ Y \\ Z \end{bmatrix} = \begin{bmatrix} 0.412453 & 0.357580 & 0.180423 \\ 0.212671 & 0.715160 & 0.072169 \\ 0.019334 & 0.119193 & 0.950227 \end{bmatrix} \begin{bmatrix} R \\ G \\ B \end{bmatrix}. \quad (28)$$

Moreover, the parameters of the CIELAB color space are calculated as follows:

$$f_{L^*}(x,y) = 116 \times h\left(\frac{Y}{Y_n}\right) - 16, \quad (29)$$

$$f_{a^*}(x,y) = 500\left[h\left(\frac{X}{X_n}\right) - h\left(\frac{Y}{Y_n}\right)\right], \quad (30)$$

$$f_{b^*}(x,y) = 200\left[h\left(\frac{Y}{Y_n}\right) - h\left(\frac{Z}{Z_n}\right)\right], \quad (31)$$

where

$$h(q) = \begin{cases} \sqrt[3]{q}, & q > 0.008856 \\ 7.787q + \dfrac{16}{116}, & \text{otherwise} \end{cases}. \quad (32)$$

Here, f_{L^*} represents the lightness from black (0) to white (100), f_{a^*} represents the lightness from green (−) to red (+), and f_{b^*} represents the lightness from blue (−) to yellow (+). The CIELAB color space was designed so that the amount of numerical change in these values corresponds to roughly the same amount of visually perceived change. Here, X_n, Y_n, and Z_n are the CIE XYZ tristimulus values of the reference white point (the subscript n suggests ''normalized'').

To classify dark defect images into foreign material and stain defects, the Euclidean distance between the defect region and background, denoted as ΔE^*_{ab}, is first calculated. Then, the just noticeable difference (JND) proposed by Weber [32] is adopted for classification. JND represents the minimum amount by which the stimulus intensity should be changed to produce a noticeable variation in the sensory experience. ΔE^*_{ab} is calculated as follows:

$$\Delta E^*_{ab} = \sqrt{(f_{L^*_b} - f_{L^*})^2 + (f_{a^*_b} - f_{a^*})^2 + (f_{b^*_b} - f_{b^*})^2}, \quad (33)$$

where $f_{L^*_b}$, $f_{a^*_b}$, and $f_{b^*_b}$ are the average values of the L^*, a^*, and b^* components of the background in the CIELAB color space, respectively.

Next, most of the stain defects are classified based on the classification rules as follows:

$$\textbf{Dark defect} = \begin{cases} \textbf{Stain}, & \Delta E_{dirt} + \textbf{JND} > \Delta E^*_{ab} \\ & > \Delta E_{dirt} - \textbf{JND} \\ \text{Undefined}, & \textbf{otherwise} \end{cases}, \quad (34)$$

where ΔE_{dirt} is the Euclidean distance between the defect region and the background of the stain defect that is precalculated by manual detection. Moreover, JND is set to 2.3 in this case.

Unfortunately, the classification rule that is based on the JND concept can only classify most of the stain defects from the image of the dark defect. However, some stain images exist in the foreign material defect group. The reason for this inaccuracy is that light transmission and reflection are different for the reflector sheet, diffuser sheet, and LGP, as shown in Fig. 12(a). In this case, a support vector machine (SVM) [33] can solve the problem in a fast and easy manner.

First, the defect image must be adaptively compensated before the defect structure analysis is conducted to compensate for the lighting of all defect images. In this case, we used the adaptive singular value decomposition (ASVD) [34] method for illumination compensation of color defect images. The singular value decomposition expression for

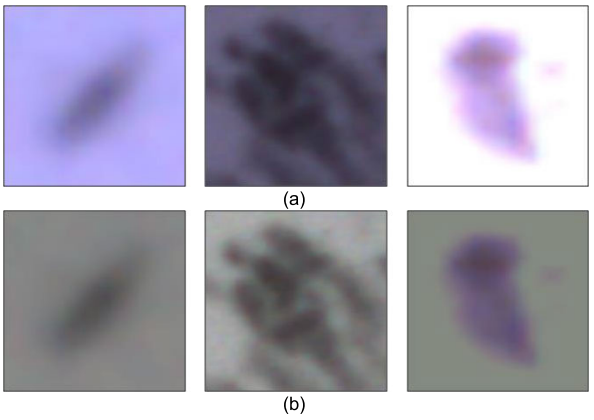

FIGURE 12. Examples of dark defect images. (a) Foreign material defect in the LGP, stain defect in the reflector sheet, and foreign material in the diffuser sheet(from left to right) and (b) respective ASVD images of (a).

each color channel of the color image can be written as follows:

$$f_A = U_A \Sigma_A V_A^T, \tag{35}$$

where U_A and V_A are orthogonal matrices with singular vectors, and $\Sigma = [D_A, O]$ contains sorted singular values (SVs) on its main diagonal. Moreover, $D_A = \text{diag}(\lambda_{A1}, \lambda_{A2}, \ldots, \lambda_{Ak})$, where λ_{Ai} represents SVs, $i = 1, \ldots,$ k in non-increasing order, O is a $k \times k$ zero matrix, and k is the rank of f_A. To reduce the influence of light variance on the defect image, the SV matrix is multiplied by the weighted compensation coefficient ρ_A to address the low contrast problem that is caused by varying light.

$$\rho_A = \frac{\mathbf{Max}\left(\Sigma_{G(\mu,\sigma)}\right)}{\mathbf{Max}(\Sigma_A),} \tag{36}$$

$$f_{CA} = U_A \left(\rho_A \Sigma_A\right) V_A^T, \tag{37}$$

where $G(\mu, \sigma)$ is the Gaussian template with a mean μ of 128 and standard deviation σ of $\sqrt{32}$. The results of the ASVD method are denoted by f_{CA}, as shown in Fig. 12(b). The defect images are observed to have the same illumination.

Next, bit-plane slicing [35] is used to extract the most significant bit (MSB) of f_{CA}, which is denoted as f_{BP} and shown in Fig. 13. The purpose of using this method is not only to extract the high-frequency signal but also to eliminate the noise interference of the background. Then, the projection color space (PCS) method [34] was used to integrate the three RGB color channels of the MSB image to reduce the within-class variance and simultaneously expand the between-class difference. The PCS P of f_{BP} can be computed as follows:

$$P = f_{BP,R} \cdot f_{BP,G}^T \cdot f_{BP,B}, \tag{38}$$

where $f_{BP,R}$, $f_{BP,G}$, and $f_{BP,B}$ are the RGB color channels obtained after using adaptive lighting compensation [34]. Moreover, "$\cdot$" is the symbol for the inner product calculation and represents the element-wise multiplication of the three matrices.

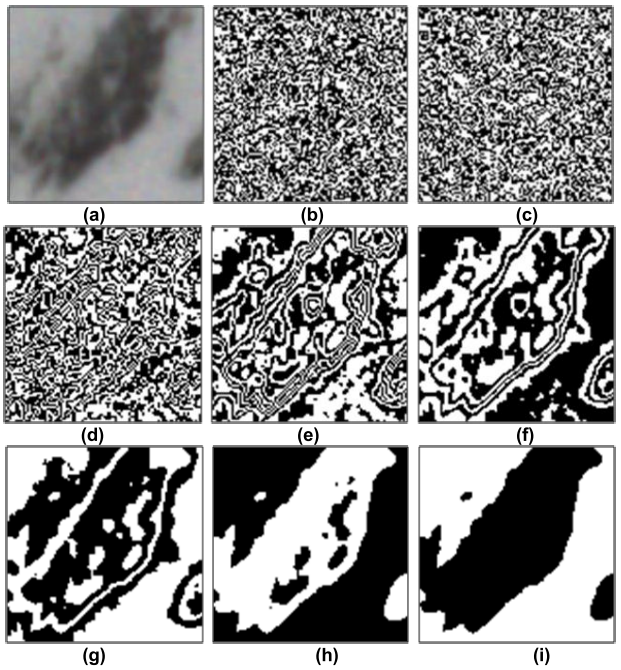

FIGURE 13. Example image of the bit-plane segmentation: (a) stain defect and(b)–(i) the lowest to the most significant bit-plane images.

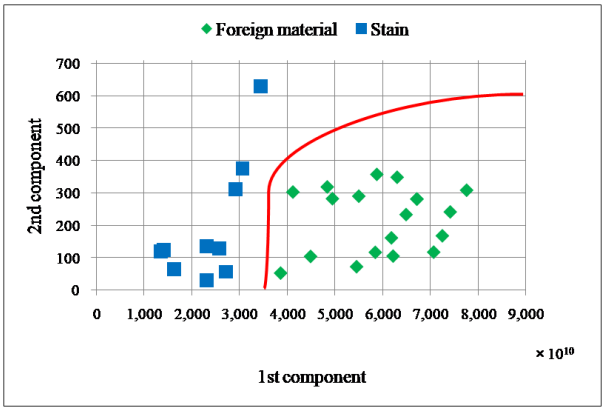

FIGURE 14. SVM classification result.

Finally, the first two singular values of P are used to form the feature vector for SVM. In this study, the RBF kernel $\exp\left(-\gamma \left\|x_i - x_j\right\|^2\right)$ was used in SVM, and the parameter γ is set to 20 with an experimental setting for SVM. The classification rule for SVM is set as follows:

$$\textbf{defect} = \begin{cases} \textbf{Foreign material}, & h(x) = 1 \\ \textbf{Stain}, & h(x) = -1 \end{cases}. \tag{39}$$

The distribution of the stain and foreign material defects by the first and second eigenvalues by using an SVM is shown in Fig. 14. As can be seen, our method can efficiently separate stain from foreign material defects.

D. CLASSIFICATION OF BRIGHT DEFECTS INTO POINT AND SCRATCH DEFECTS

As discussed in Section IV.C, the color space and SVM can be used to further classify the dark defects into foreign

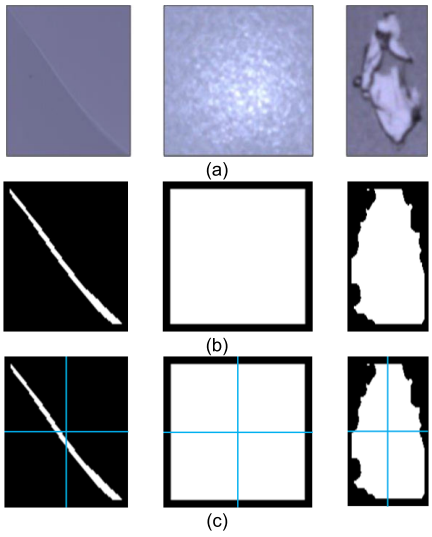

FIGURE 15. Classification of bright defects: (a) Bright defect images, (b) separation of the defect region from the background, and (c) division of the defect image into four equal parts.

material and stain defect categories. However, this method is not effective for classifying the bright defect images into the point and scratch defect categories. This section presents a method that classifies defect images based on the shape.

First, the defect region is separated from the background of the defect image f that has a size of m× n by using the Kirsch operator, and the edge of the defect is detected. Then, the adaptive energy analysis is used to enhance the defect contour, as discussed in Section IV.B. Here, the white color (grayscale value: 255) is set for the points within the defect region, and black color (grayscale value: 0) is set for the background, as presented in Fig. 15(b). The image in this step is denoted as $\boldsymbol{f_B}$. Then, the image $\boldsymbol{f_B}$ image is divided into four equal parts along two axes through the center of the defect image and perpendicular to the edges, as shown in Fig. 15(c).

The classification of scratch and point defects is conducted by calculating and comparing the ratio among the average grayscale values of the four equal parts as follows:

$$\boldsymbol{q_A} = \sum_{i=0}^{m-1}\sum_{j=0}^{n-1} \boldsymbol{f_B}(\boldsymbol{i},\boldsymbol{j}), \tag{40}$$

$$\boldsymbol{q_1} = \frac{1}{\boldsymbol{q_A}} \times \sum_{i=\frac{m}{2}}^{m-1}\sum_{j=0}^{\frac{n}{2}-1} \boldsymbol{f_B}(\boldsymbol{i},\boldsymbol{j}) \times 100\%, \tag{41}$$

$$\boldsymbol{q_2} = \frac{1}{\boldsymbol{q_A}} \times \sum_{i=0}^{\frac{m}{2}-1}\sum_{j=0}^{\frac{n}{2}-1} \boldsymbol{f_B}(\boldsymbol{i},\boldsymbol{j}) \times 100\%\,, \tag{42}$$

$$\boldsymbol{q_3} = \frac{1}{\boldsymbol{q_A}} \times \sum_{i=0}^{\frac{m}{2}-1}\sum_{j=\frac{n}{2}}^{n-1} \boldsymbol{f_B}(\boldsymbol{i},\boldsymbol{j}) \times 100\%, \tag{43}$$

$$\boldsymbol{q_4} = \frac{1}{\boldsymbol{q_A}} \times \sum_{i=\frac{m}{2}}^{m-1}\sum_{j=\frac{n}{2}}^{n-1} \boldsymbol{f_B}(\boldsymbol{i},\boldsymbol{j}) \times 100\%, \tag{44}$$

where $\boldsymbol{q_A}$ is represents the average grayscale values of $\boldsymbol{f_B}$ and $\boldsymbol{q_i}$, $\boldsymbol{i}$= **1, 2, 3, 4,** is the average percentage of the $\boldsymbol{i}^{\text{th}}$ quadrant that is referred to as $\boldsymbol{q_A}$. Based on our observation, the defect region of point defects is usually distributed across all four parts of the defect image, whereas the scratch defect is usually present in only one or two quadrants of the image. Moreover, A and B set with $\boldsymbol{q_i}$, **where** $\boldsymbol{i} = \mathbf{1, 2, 3, 4,}$ that are defined as follows:

$$\boldsymbol{A} = \{\boldsymbol{q_i} > \mathbf{0.25}, \boldsymbol{i} = \mathbf{1, 2, 3, 4,}\} \tag{45}$$

$$\boldsymbol{\mu_A} = \frac{1}{\boldsymbol{n(A)}} \sum_{\boldsymbol{q_i} \in \boldsymbol{A}} \boldsymbol{q_i}, \tag{46}$$

$$\boldsymbol{B} = \{\boldsymbol{q_i} \leq \mathbf{0.25}, \boldsymbol{i} = \mathbf{1, 2, 3, 4,}\} \tag{47}$$

where $\boldsymbol{\mu}_{\mathrm{A}}$ is the average value of all elements in set A, and $\boldsymbol{n}$ $(\boldsymbol{A})$ is the element number of A. The classification of point and scratch defects is conducted as follows:

$$\textbf{Bright defect} = \begin{cases} \textbf{scratch}, & \textbf{if } \boldsymbol{n}(\boldsymbol{A}) \geq \mathbf{2} \ \textit{and} \\ & (\boldsymbol{b} < \frac{1}{2}\boldsymbol{\mu}_{\mathrm{A}}, \forall \boldsymbol{b} \in \boldsymbol{B}) \\ \textbf{point}, & \textbf{otherwise} \end{cases}. \tag{48}$$

V. EXPERIMENTAL RESULT AND DISCUSSION

In this section, the defect detection and classification algorithms are tested on four types of optical films with a total of 120 samples provided by a manufacturer in Taiwan. The following are the specifications of the sheets used: reflector sheet size: 354 × 197mm^2 with a total of 22 samples, LGP size: 354 × 197mm^2 with a total of 19 samples, diffuser sheet size: 177× 110mm^2 with a total of 24 samples, and diffuser sheet size: 157 × 92 mm^2 with a total of 21 samples.

A. IMAGE ACQUISITION PARAMETERS

The acquisition equipment system is displayed in Fig. 3. The proposed system was implemented in Microsoft Visual Studio C# 2010. The experiments were conducted on a PC equipped with an Intel Core i7-4790 CPU@3.60GHz, RAM DDR3 8GB, with a Windows 10 operating system.

The system employed a camera (avA2300-30kc, Basler, Germany) with a camera-link interface and a KAI-4050 charge-coupled device sensor to provide 31 frames per second at a resolution of 4 MP. The sensor has a size of 12.8 × 9.6 mm^2, resolution (H×V) of 2330 × 1750 pixels, and pixel size (H×V) of 5.5 × 5.5 μm^2. The camera adapted a 60-mm microlens that had an aperture of 2.8 (Nikon, Japan). This lens is an excellent normal and short telephoto lens and an exceptional close-up lens, which focuses on life-size. Thus, an object with a diameter of an inch can occupy an entire frame. The light source used was PHILIPS Ambiance Globe 17W E27 Cool daylight. The distances between the camera, light source, and optical films are listed in Table 1.

B. OPTICAL FILM DEFECT DETECTION RESULT

To inspect whether the optical film satisfies the requirement of the manufacturer, the region of interest on an optical film was located and extracted first.

TABLE 1. The distance between the objects and the image acquisition system.

Optical film type	The distance between two objects		
	Backlightto sample	Front light to sample	CCD Camera to sample
Reflector	245 mm	-	190 mm
Light guide plate	-	30 mm	190 mm
Diffuser	-	30 mm	190 mm

TABLE 2. Averagedefect detection rate and operation time.

Optical film type	Defect detection rate	Pass / No pass decision time	Total running time
Reflector	100%	0.867s / pc.	8.179s / pc.
Light guide plate	100%	0.891s / pc.	5.991s / pc.
Diffuser	98.7%	0.768s / pc.	4.218s / pc.

To reduce the processing time, the color image was transformed into the YCbCr color space to obtain the Y channel image for contour extraction. Based on the localized energy analysis of the Y channel image, the defects were extracted one by one by using cross-projection in both the horizontal and vertical directions, as discussed in Section III. The size and number of the defects were then calculated to check whether the manufacturer's specification requirement is satisfied. Then, the object undergoes the classification process to decide whether it can achieve the quality standards or not. The detailed algorithm is discussed in Section IV, and the results of the defect images detected using our proposed method are presented in Fig. 16.

In our experiments, we achieved a defect detection rate of 100% for the reflector sheets and LGP and achieved a rate of 98.7% for the diffuser sheets. The reason for the lower detection rate for diffuser sheets is that there are five low-quality sheets. The defect on one sheet cannot be detected with the human eye and can only be detected through tactile sense. The average time for manual defect detection is 14.624 s/piece, which is much longer than the average time required by the proposed system (6.129s/piece). The defect detection rate, Pass/No pass decision time, and the total operation time are presented in Table 2 to demonstrate the effectiveness of our method.

C. OPTICAL FILM DEFECT CLASSIFICATION RESULT

After detection, the defect images undergo the process to classify the image into four categories—point, scratch, foreign material, and stain. The proposed algorithm classifies the defect image into two categories—dark and bright. The dark category includes foreign material and stain defects, whereas the bright category includes point and scratch defects. First, the defects are classified into dark and bright categories by analyzing whether the horizontal line passes through the center of the defect, as shown in Fig. 17. Before classification, the defect region is extracted, and the background in the defect image is removed using the Kirsch operator and energy analysis, as shown in Fig. 18.

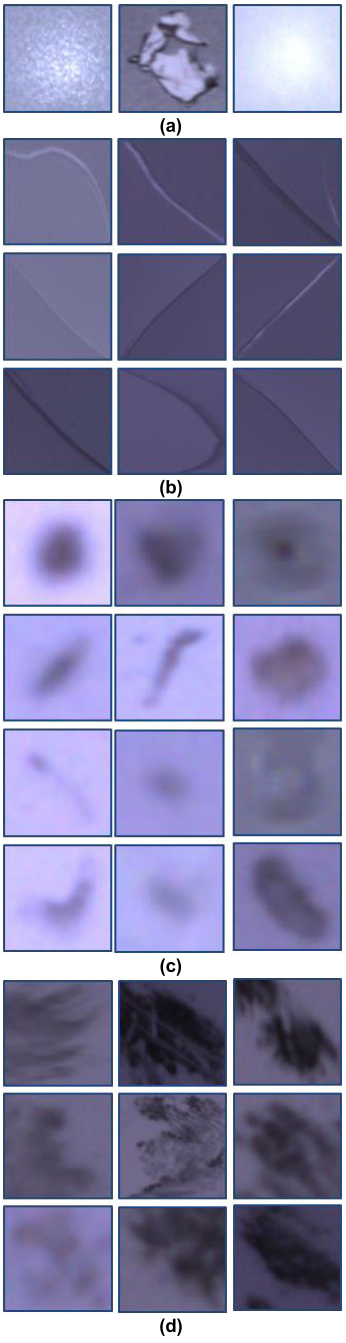

FIGURE 16. Result of defect detection with the proposed method: (a) point, (b) scratch, (c) foreign material, and (d) stain.

For the dark category, most of the stain defects are obtained by computing and comparing the Euclidean distance between

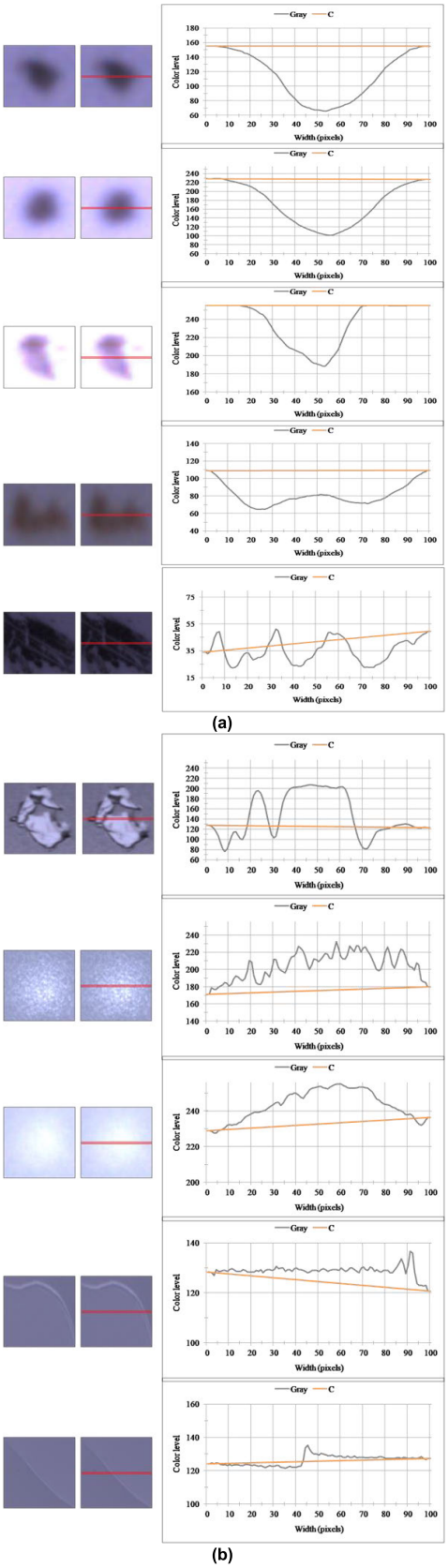

FIGURE 17. Classification based on analyzing the distribution of the defect center: (a) dark defects and(b) light defects.

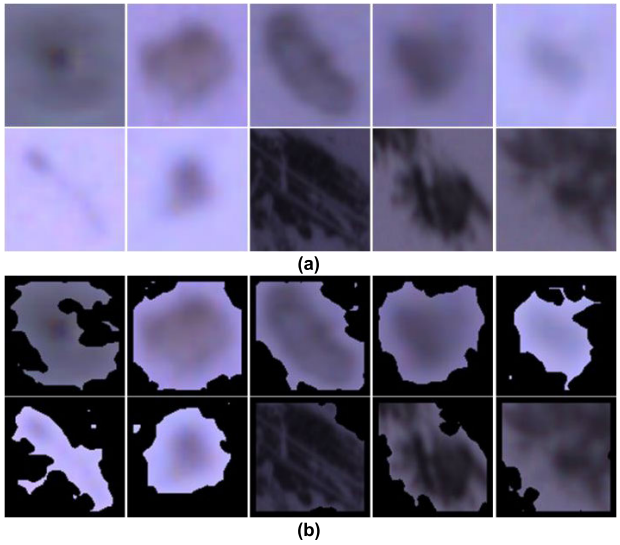

FIGURE 18. (a) Dark defect samples and (b) result after background removal.

the defect region and the background of the defect images in the CIELAB color space. The remaining defect images are enhanced using the ASVD method. Then, the MSB images are extracted for SVM classification. The ASVD images and MSB images of dark defects are shown in Fig. 19.

For the bright defect images, the defect region sare extracted, and the background in the defect image is removed by using the Kirsch operator and adaptive energy analysis, as shown in Fig. 20. Then, the defect image is divided into four equal parts. Finally, the ratio between the average grayscale values of the four equal parts is calculated to classify the bright defect images into scratch and point defects. Our classification method has a classification accuracy rate of 100%.

To show the effectiveness of our proposed method, we did more experiments by using the supervised machine learning technique for defect classification. Support Vector Machines (SVM) is a supervised learning technique that is used to develop predictive models for classification. Recently, SVM has been widely used in defects classification [36]–[38]. In our problem, we classified the defects into four categories by using the LIBSVM library [39] which supports multi-class SVM classification. We used the histogram of oriented gradients (HOG) descriptors [40] as a feature vector for SVM and the radial basis function kernel $\exp(-\gamma||x_i - x_j||^2)$, where γ is a parameter that sets the ''spread'' of the kernel, x_i and x_j are represented as feature vectors in input space. However, we only got a 94% true classification rate. This is caused by using different sizes of defects, illumination, types of optical films. Besides, the classification using SVM also depends heavily on the scale, parameter γ, and function kernel for each database.

The results reveal that the proposed system can detect and classify defects in optical films with high efficiency even when the size of a defect is very small and cannot be

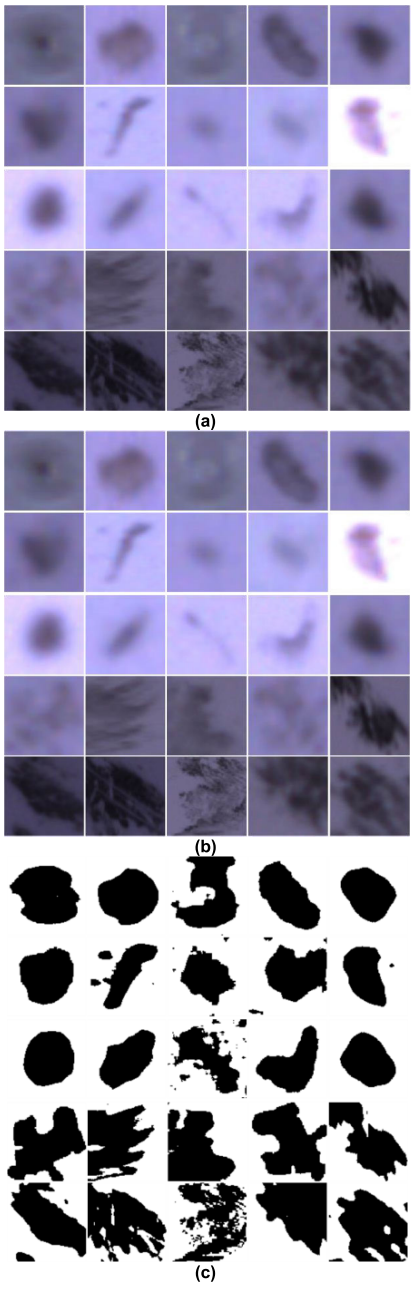

FIGURE 19. (a) Dark defects, (b) ASVD images of (a), (c) segmented images of the MSB plane in (b).

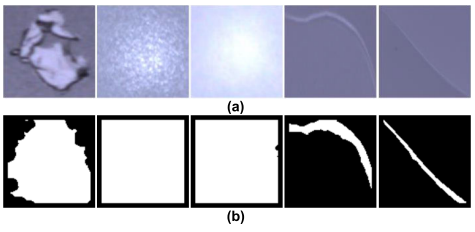

FIGURE 20. (a) Dark defects and (b) separationof the defect region fromthe background.

seen clearly by human eyes. Moreover, the operation time is short; thus, the proposed framework can fully meet the manufacturer's requirements.

VI. CONCLUSION

We proposed an effective OFDDCS in this study that has three sections. The first section includes an optical structure for image acquisition that can remove environmental lighting interference and then highlight defects. The second section includes an efficient algorithm based on adaptive energy analysis with cross-projection for detecting the defects on the optical film. Finally, an efficient classification algorithm has been proposed to classify the defects into four types—point, scratch, foreign material, and stain defects. The experiments were conducted on 120 optical film samples provided by a manufacturer in Taiwan. The results revealed that the proposed system can provide a 99.6% defect detection rate and a 100% classification accuracy rate. Moreover, only 6.129s are required on average to perform the inspection for an optical film sample.

ACKNOWLEDGMENT

The authors would like to thank WahHong Company, Ltd, Taiwan, for their joint development of the inspection system.

REFERENCES

[1] K. Kaur, "Various techniques for PCB defect detection," *Int. J. Eng. Sci.*, vol. 17, pp. 175–178, Jan. 2016.
[2] W.-C. Wang, S.-L. Chen, L.-B. Chen, and W.-J. Chang, "A machine vision based automatic optical inspection system for measuring drilling quality of printed circuit boards," *IEEE Access*, vol. 5, pp. 10817–10833, 2017.
[3] P. Wei, C. Liu, M. Liu, Y. Gao, and H. Liu, "CNN-based reference comparison method for classifying bare PCB defects," *J. Eng.*, vol. 2018, no. 16, pp. 1528–1533, Nov. 2018.
[4] W. Michaeli, "Inline inspection of textured plastics surfaces," *Opt. Eng.*, vol. 50, no. 2, Feb. 2011, Art. no. 027205.
[5] J. P. Yun, D. Kim, K. Kim, S. J. Lee, C. H. Park, and S. W. Kim, "Vision-based surface defect inspection for thick steel plates," *Opt. Eng.*, vol. 56, no. 5, May 2017, Art. no. 053108.
[6] Q. Luo and Y. He, "A cost-effective and automatic surface defect inspection system for hot-rolled flat steel," *Robot. Comput.-Integr. Manuf.*, vol. 38, pp. 16–30, Apr. 2016.
[7] X. Zhou, Y. Wang, C. Xiao, Q. Zhu, X. Lu, H. Zhang, J. Ge, and H. Zhao, "Automated visual inspection of glass bottle bottom with saliency detection and template matching," *IEEE Trans. Instrum. Meas.*, vol. 68, no. 11, pp. 4253–4267, Nov. 2019.
[8] Q. Liang, S. Xiang, J. Long, W. Sun, Y. Wang, and D. Zhang, "Real-time comprehensive glass container inspection system based on deep learning framework," *Electron. Lett.*, vol. 55, no. 3, pp. 131–132, Feb. 2019.
[9] D.-M. Tsai, G.-N. Li, W.-C. Li, and W.-Y. Chiu, "Defect detection in multi-crystal solar cells using clustering with uniformity measures," *Adv. Eng. Informat.*, vol. 29, no. 3, pp. 419–430, Aug. 2015.
[10] Y. Chiou, J. Liu, and Y. Liang, "Micro crack detection of multi–crystalline silicon solar wafer using machine vision techniques," *Sensor Rev.*, vol. 31, no. 2, pp. 154–165, Mar. 2011.
[11] A. Kumar, "Computer-Vision-Based fabric defect detection: A survey," *IEEE Trans. Ind. Electron.*, vol. 55, no. 1, pp. 348–363, Jan. 2008.
[12] M. Bahaghighat, L. Akbari, and Q. Xin, "A machine learning-based approach for counting blister cards within drug packages," *IEEE Access*, vol. 7, pp. 83785–83796, 2019.
[13] J. Xu, Y. Liu, H. Xie, and F. Luo, "Surface quality assurance method for lithium-ion battery electrode using concentration compensation and partiality decision rules," *IEEE Trans. Instrum. Meas.*, early access, Jul. 29, 2019, doi: 10.1109/TIM.2019.2929670.
[14] Y. Deng, X. Pan, X. Wang, and X. Zhong, "Vison-based 3D shape measurement system for transparent microdefect characterization," *IEEE Access*, vol. 7, pp. 105721–105733, 2019.
[15] C.-F.-J. Kuo, C.-Y. Lai, C.-H. Kao, and C.-H. Chiu, "Integrating image processing and classification technology into automated polarizing film defect inspection," *Opt. Lasers Eng.*, vol. 104, pp. 204–219, May 2018.

[16] W.-W. Lai, X.-X. Zeng, J. He, and Y.-L. Deng, "Aesthetic defect characterization of a polymeric polarizer via structured light illumination," *Polym. Test.*, vol. 53, pp. 51–57, Aug. 2016.
[17] Y. Gan and Q. Zhao, "An effective defect inspection method for LCD using active contour model," *IEEE Trans. Instrum. Meas.*, vol. 62, no. 9, pp. 2438–2445, Sep. 2013.
[18] J. Z. Tsai, R.-S. Chang, and T.-Y. Li, "Detection of gap mura in TFT LCDs by the interference pattern and image sensing method," *IEEE Trans. Instrum. Meas.*, vol. 62, no. 11, pp. 3087–3092, Nov. 2013.
[19] T.-Y. Li, J.-Z. Tsai, R.-S. Chang, L.-W. Ho, and C.-F. Yang, "Pretest gap mura on TFT LCDs using the optical interference pattern sensing method and neural network classification," *IEEE Trans. Ind. Electron.*, vol. 60, no. 9, pp. 3976–3982, Sep. 2013.
[20] J.-W. Wang, W.-Y. Chen, and J.-S. Lee, "Singular value decomposition combined with wavelet transform for LCD defect detection," *Electron. Lett.*, vol. 48, no. 5, p. 266, 2012.
[21] W.-C. Li and D.-M. Tsai, "Defect inspection in low-contrast LCD images using Hough transform-based nonstationary line detection," *IEEE Trans Ind. Informat.*, vol. 7, no. 1, pp. 136–147, Feb. 2011.
[22] L.-F. Chen, C.-T. Su, and M.-H. Chen, "A neural-network approach for defect recognition in TFT-LCD photolithography process," *IEEE Trans. Electron. Packag. Manuf.*, vol. 32, no. 1, pp. 1–8, Jan. 2009.
[23] X. Bi, C. Zhuang, and H. Ding, "A new mura defect inspection way for TFT-LCD using level set method," *IEEE Signal Process. Lett.*, vol. 16, no. 4, pp. 311–314, Apr. 2009.
[24] S.-L. Chen and S.-T. Chou, "TFT-LCD mura defect detection using wavelet and cosine transforms," *J. Adv. Mech. Des., Syst., Manuf.*, vol. 2, no. 3, pp. 441–453, 2008.
[25] J. Y. Lee and S. I. Yoo, "Automatic detection of region-mura defect in TFT-LCD," *IEICE Trans. Inf. Syst.*, vol. 87, no. 10, pp. 2371–2378, 2004.
[26] N. Otsu, "A threshold selection method from gray-level histograms," *IEEE Trans. Syst., Man, Cybern.*, vol. 9, no. 1, pp. 62–66, Jan. 1979.
[27] R. C. Gonzalez and R. E. Woods, *Digital Image Processing*, 3rd ed. Englewood Cliffs, NJ, USA: Prentice-Hall, 2008.
[28] S. Lu, Z. Wang, and J. Shen, "Neuro-fuzzy synergism to the intelligent system for edge detection and enhancement," *Pattern Recognit.*, vol. 36, no. 10, pp. 2395–2409, Oct. 2003.
[29] D.-S. Lu and C.-C. Chen, "Edge detection improvement by ant colony optimization," *Pattern Recognit. Lett.*, vol. 29, no. 4, pp. 416–425, Mar. 2008.
[30] R. A. Kirsch, "Computer determination of the constituent structure of biological images," *Comput. Biomed. Res.*, vol. 4, no. 3, pp. 315–328, Jun. 1971.
[31] A. Levinshtein, A. Stere, K. N. Kutulakos, D. J. Fleet, S. J. Dickinson, and K. Siddiqi, "TurboPixels: Fast superpixels using geometric flows," *IEEE Trans. Pattern Anal. Mach. Intell.*, vol. 31, no. 12, pp. 2290–2297, Dec. 2009.
[32] *Weber's Law of Just Noticeable Difference*. Accessed: Jan. 13, 2020. [Online]. Available: https://en.wikipedia.orgwiki/Just-noticeable_difference
[33] C. Cortes and V. Vapnik, "Support-vector networks," *Mach. Learn.*, vol. 20, no. 3, pp. 273–297, 1995.
[34] J.-W. Wang, J.-S. Lee, and W.-Y. Chen, "Face recognition based on projected color space with lighting compensation," *IEEE Signal Process. Lett.*, vol. 18, no. 10, pp. 567–570, Oct. 2011.
[35] H. Noda, J. Spaulding, M. N. Shirazi, and E. Kawaguchi, "Application of bit-plane decomposition steganography to JPEG2000 encoded images," *IEEE Signal Process. Lett.*, vol. 9, no. 12, pp. 410–413, Dec. 2002.
[36] D. J. Pasadas, P. Baskaran, H. G. Ramos, and A. L. Ribeiro, "Detection and classification of defects using ECT and multi-level SVM model," *IEEE Sensors J.*, vol. 20, no. 5, pp. 2329–2338, Mar. 2020.
[37] D. Wang, L. Zhou, C. Dai, L. Guo, and W. Liao, "Insulation defect diagnostic method for OIP bushing based on multiclass LS-SVM and cuckoo search," *IEEE Trans. Instrum. Meas.*, vol. 69, no. 1, pp. 163–172, Jan. 2020.
[38] X. Yuan, Z. Liu, Z. Miao, Z. Zhao, F. Zhou, and Y. Song, "Fault diagnosis of analog circuits based on IH-PSO optimized support vector machine," *IEEE Access*, vol. 7, pp. 137945–137958, 2019.
[39] C.-C. Chang and C.-J. Lin, "LIBSVM: A library for support vector machines," *ACM Trans. Intell. Syst. Technol.*, vol. 2, no. 3, pp. 1–27, Apr. 2011.
[40] N. Dalal and B. Triggs, "Histograms of oriented gradients for human detection," in *Proc. IEEE Comput. Soc. Conf. Comput. Vis. Pattern Recognit. (CVPR)*, San Diego, CA, USA, Jun. 2005, pp. 886–893.

NGOC TUYEN LE received the B.S. degree in mathematics and information from the Hanoi National University of Education, Hanoi, Vietnam, in 1996, the M.S. degree in computer science from Le Qui Don Technical University, Hanoi, in 2006, and the Ph.D. degree in electrical engineering from the National Kaohsiung University of Science and Technology, Taiwan, in 2015. He is currently a Postdoctoral Researcher with the Institute of Photonics Engineering, National Kaohsiung University of Science and Technology. His research interests include digital image processing, automatic optical inspection systems, face recognition, and fingerprint classification.

JING-WEIN WANG received the B.S. and M.S. degrees in electrical engineering from the National Taiwan University of Science and Technology, in 1986 and 1988, respectively, and the Ph.D. degree in electrical engineering from National Cheng Kung University, Taiwan, in 1998. He was the Chief Project Leader with the Equipment Design Center, PHILIPS, Taiwan, from 1992 to 2000. He joined the Faculty Member of the National Kaohsiung University of Science and Technology, in 2000, and assumed duties as the Dean of the College of Electrical Engineering and Information Science, from 2017 to 2019. He is currently a Distinguished Professor with the Institute of Photonics Engineering. His current research interests include combinatorial optimization, pattern recognition, and wavelets and their applications.

MENG-HSIANG SHIH received the B.S. degree in information and management from Nanhua University, Taiwan, in 2001. He is currently pursuing the Ph.D. degree with the National Kaohsiung University of Science and Technology, Taiwan. He is very good at using computer skills to find solutions, especially the applications in the IT industry. On the other hand, he is a professional manager in school, and his main tasks including the project management and planning proposal, implementing industry–academia collaboration objects, offering solutions for teachers and business cooperation, and provide teachers research and development results to promote knowledge economic development. His research interests include digital imageprocessing, automatic optical inspection systems, algorithms, and information technology.

CHOU-CHEN WANG received the B.S. and M.S. degree in electrical engineering from the National Defense University, Taoyuan, Taiwan, in 1988 and 1992, respectively, and the Ph.D. degree in electrical engineering from National Cheng Kung University, Tainan, Taiwan, in 1999. He is currently a Professor with the Department of Electrical Engineering, I-Shou University, Kaohsiung, Taiwan. His current research interests include intelligent video analytics, digital signal processing, image and video coding standards, and communication systems.